Fast imaging of transients and coherent magnetohydrodynamic modes in DIII-D[a)]

J. H. Yu,[1,b)] M. A. Van Zeeland,[2] M. S. Chu,[2] V. A. Izzo,[1] and R. J. La Haye[2]
[1]*University of California at San Diego, La Jolla, California 92093, USA*
[2]*General Atomics, P.O. Box 85608, San Diego, California 92186-5608, USA*

(Received 18 December 2008; accepted 24 March 2009; published online 30 April 2009)

A fast framing camera is used to image plasma waves and instabilities in the DIII-D tokamak [J. L. Luxon, Nucl. Fusion **42**, 614 (2002)] in unprecedented detail including tearing modes (TMs) and sawtooth crashes. To image core magnetohydrodynamic (MHD) activity, the fast camera detects visible bremsstrahlung emission ε_B in moderate to high density plasmas. For coherent MHD activity such as TMs, high-resolution two-dimensional images of mode amplitude and phase are obtained by Fourier filtering each pixel's time series at the mode frequency. Images of $m/n=2/1$ TMs show that inside the $q=2$ surface, the camera measurements are in excellent agreement with an analytic model of a 2/1 island superimposed on the equilibrium ε_B profile. Direct comparison of the measurements to a NIMROD simulation shows significant discrepancies, most likely due to artificially high-density diffusion used in the code for numerical stability. The first visible-light images of transient sawtooth crashes show the structure and location of the perturbed emission from an $m=1$ precursor oscillation and show that during the nonlinear crash phase the instability extends to more than half of the plasma minor radius. © *2009 American Institute of Physics*. [DOI: 10.1063/1.3118626]

I. INTRODUCTION

Magnetohydrodynamic (MHD) activity in the core of tokamaks is an important area of research because instabilities and coherent modes can lower the normalized plasma pressure and reduce fusion performance. While fast framing visible cameras are typically used to study edge physics in tokamaks including edge localized modes (ELMs),[1–3] edge turbulence,[4] and dust dynamics,[5,6] here we present fast framing camera images of core MHD mode structure and dynamics by detecting visible bremsstrahlung emission ε_B in the DIII-D tokamak. The ability to visualize ε_B in the core of the plasma using fast cameras allows the study of MHD waves and instabilities in unprecedented detail.

One type of resistive mode that is a particular concern for the International Thermonuclear Experimental Reactor (ITER) is the tearing mode (TM),[7,8] which can persist for thousands of mode periods while reducing β before potentially terminating the plasma in a disruption, where β is defined as the ratio of volume averaged plasma pressure to magnetic field pressure. The TM is a magnetic island chain that forms when magnetic field lines break and reconnect at a rational magnetic flux surface. Within the island the pressure is locally flattened, which reduces the pressure gradient and the neoclassical bootstrap current. The lack of bootstrap current within the island creates a helical perturbation to the total plasma current, which can further drive the instability by increasing the width of the island and by further reducing the pressure gradient. When the islands are sustained by the perturbed bootstrap current, these modes are called neoclassical tearing modes (NTMs).

Transient MHD events such as sawtooth instabilities can produce the seed island required for NTM growth and can trigger other MHD events such as ELMs; in addition, large sawtooth crashes themselves can lead to significant loss of stored plasma energy.[9] In ITER, sawteeth may be important because they are expected to redistribute fusion alpha particles and may have the beneficial effect of removing helium ash from the plasma core. The sawtooth instability forms when the plasma current is peaked near the magnetic axis, creating a region in the core where the safety factor q is less than unity. During the sawtooth crash, plasma from the core is rapidly (~ 100 μs) mixed with the outer regions, causing cooling of the plasma near the magnetic axis. After the crash, the central temperature gradually rises as the current profile and fast ion population evolve, and the process repeats. The exact nature of the magnetic reconnection that occurs during the sawtooth crash has eluded a complete physics explanation, and fast imaging of these events may provide new insights through detailed comparison to theory.

Traditional diagnostics of the structure and dynamics of these core MHD events include soft x-ray detectors,[10,11] electron cyclotron emission (ECE) measurements including linear and two-dimensional (2D) arrays,[12] and magnetic Mirnov probes. These measurements provide high quality data with fast sample rates (>100 kHz) but are often limited in spatial resolution and coverage. The views available for fast visible cameras, on the other hand, are limited only by port access since interchanging objective lenses is trivial. These cameras produce high-resolution data with broad coverage and are proving to be valuable diagnostic tools.

In this article, Sec. II describes the experimental setup and the camera viewing geometry. The measurements of TM structure through temporal Fourier filtering and comparison to modeling, including nonlinear resistive NIMROD modeling, are presented in Sec. III. The fast camera is used to measure

[a)]Paper TI2 4, Bull. Am. Phys. Soc. **53**, 241 (2008).
[b)]Invited speaker.

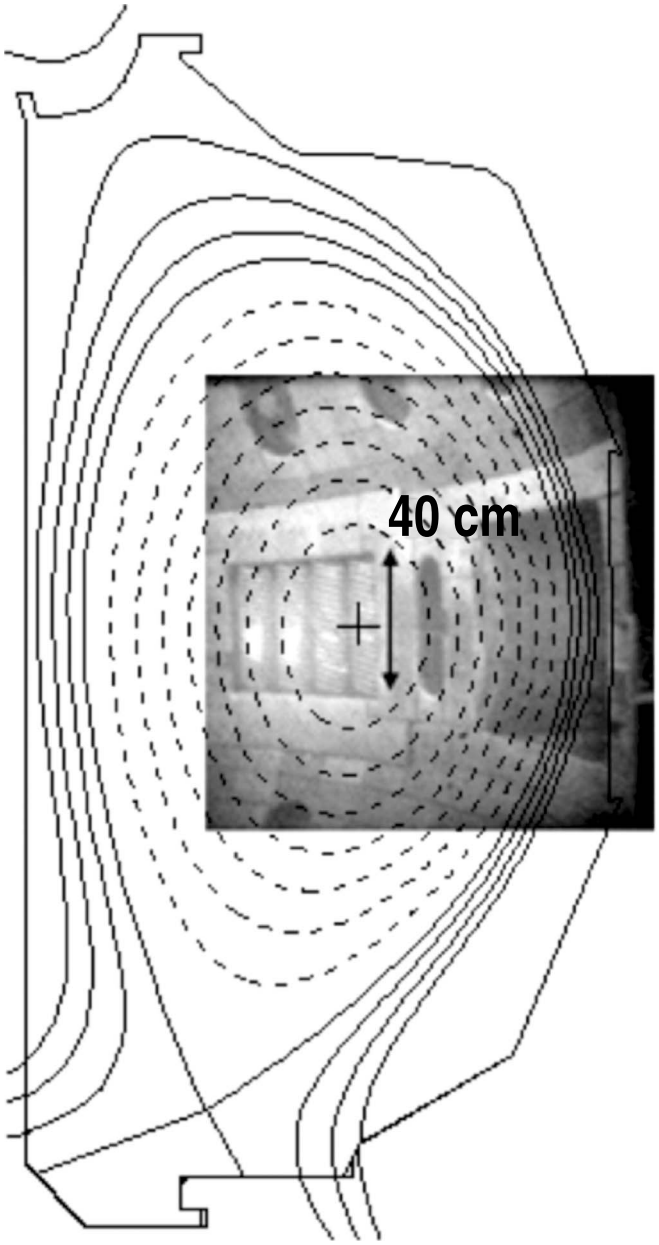

FIG. 1. Camera view inside the DIII-D vacuum vessel showing a typical field of view relative to the full plasma cross section. 40 cm refers to the vertical distance at the wall.

the island width, complementing the use of magnetics and ECE. We find that the saturated island width of a TM is up to 30% of the plasma minor radius, and that as expected, the mode phase reverses at the island location. Section IV describes the first visible light images of a sawtooth crash and shows that the perturbed emission extends to over half of the plasma minor radius during the nonlinear temperature collapse. Concluding remarks are given in Sec. V.

II. EXPERIMENTAL CONFIGURATION

The DIII-D tokamak is well documented elsewhere.[13] As seen in Fig. 1, the fast framing visible camera views a midplane region of the plasma with sightlines directed tangentially along the toroidal direction. The field of view ranges from approximately half to nearly all of the plasma cross section, depending on the optics and the user-defined active area of the camera detector. The vertical field of view is limited by the viewing port to $\sim 1/3$ of the vertical extent of the plasma. The Phantom v7.1 (Vision Research, Inc.) camera has a complementary metal-oxide semiconductor detector with 12-bit dynamic range and 22×22 μm^2 pixel area. The maximum resolution is 800×600 pixels; however, high frame rates require the use of a subset of the detector chip and the typical resolution presented here is 256×256 pixels, corresponding to a maximum frame rate of 2.6×10^4 frames/s. When plasma dynamics are slow enough, the signal can be increased by increasing the exposure time, and a frame rate of 1.0×10^4 frames/s is also used here. No optical filter is used in order to maximize the signal and the detected wavelengths range from 450–950 nm with a peak spectral response near $\lambda = 700$ nm.[14] Each pixel images an area in the plasma core of $\sim 3\times 3$ mm^2 at the point of tangency between the pixel's sightline and a magnetic flux surface.

The signal received by a pixel in the camera detector is the integrated emission from plasma volume elements along the pixel's sightline. The data presented here are not inverted, and thus line integration effects are retained in the camera images. One possible limitation caused by line integration is that instabilities with rapid variation along the direction of the sightline cannot be clearly imaged due to phase cancellation. We estimate that this phase cancellation would limit imaging core MHD in our system for $n>8$, where n is the toroidal mode number. In this paper, however, we focus on low mode number instabilities with $n=1$. Another line integration effect is that the camera-detected mode structure appears spatially extended and less localized to a flux surface compared to the true mode structure at a single poloidal plane. This effect becomes more pronounced on the high field side.

III. MEASUREMENTS AND MODELING OF 2D TM STRUCTURE

TM islands can grow at rational surfaces $q=m/n$ (m is the poloidal mode number) due to free energy available from the current profile in a linearly unstable plasma (classical TM) or can be driven nonlinearly unstable by the helically perturbed bootstrap current (NTM). After the initial growth phase of either a classically unstable TM or of a classically stable nonlinearly unstable NTM, the islands modify the equilibrium and the plasma transitions to the nonlinear "saturated" state. The saturated or slowly evolving islands are thus maintained by either the island modification of the classical tearing stability and/or the helically perturbed bootstrap current.

A. Correlation between camera and magnetics

A high degree of cross power and coherence between the signal from camera pixels (viewing a midplane region near $\rho=0.4$) and the signal from a Mirnov coil is detected when a TM with poloidal and toroidal mode numbers $m/n=2/1$ exists in the plasma, as shown in Fig. 2. The cross power measures the degree of spectral overlap or correlation in the fre-

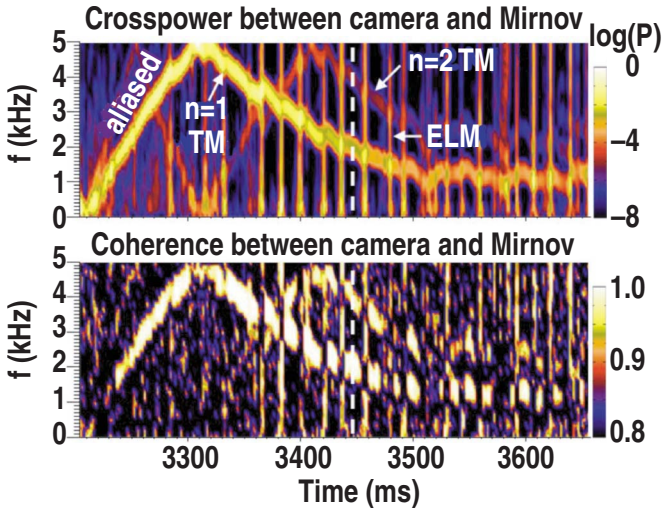

FIG. 2. (Color online) Cross power and coherence between the camera signal (from a region near the midplane $q=2$ surface) and magnetic Mirnov signal (mapped to the same time base as the camera frame rate) for shot 133 454. The 2/1 TM frequency decreases due to mode coupling to the wall, which drags on the mode and slows the rotation.

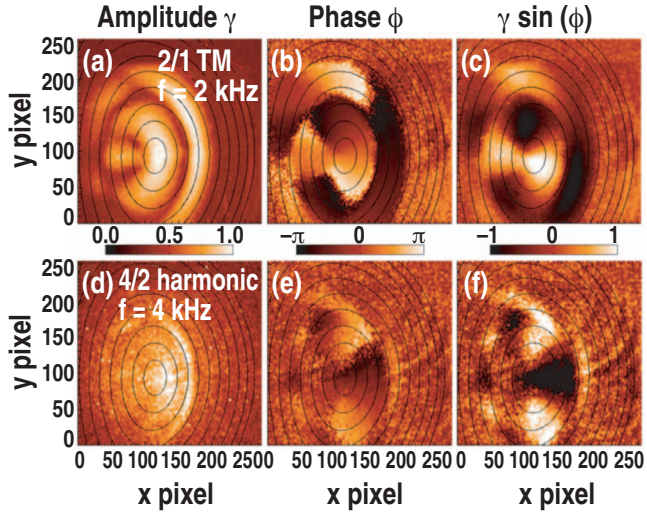

FIG. 3. (Color) The line-integrated (a) Fourier amplitude, (b) phase, and (c) a mode snapshot obtained by Fourier filtering each pixel's time series at the 2/1 mode frequency $f=2$ kHz. (d)–(f) show Fourier images obtained by filtering at the harmonic frequency $f=4$ kHz, showing the $m=4$ structure of the harmonic. Overlaid are contours of the square root of normalized toroidal flux ρ mapped to the point of tangency for each pixel's sightline, with ρ ranging from 0.1 to 1.0 in equal increments.

quency domain between two signals, and coherence is the cross power normalized to the square root of the product of each signal's autopower. At the $n=1$ mode frequency, both the cross power and coherence between the camera signal and magnetic Mirnov probe signal are high, indicating that the emission detected by the camera exhibits fluctuations due to the mode. The one-dimensional camera signal used here is obtained by summing for each frame the intensity from a 10×10 subset of pixels with lines of sight which are approximately tangent to the $q=2$ surface at the midplane. The Mirnov signal has been mapped to the same time base as the camera signal, which is aliased for frequencies satisfying $f>f_{Nyq}=5$ kHz. The H-mode discharge presented here has toroidal magnetic field $B_T=1.6$ T, reversed plasma current $I_p=1.0$ MA, neutral beam (NB) heating power of 12 MW, central electron temperature $T_e=1.9$ keV, and central density $n_e=5.0\times10^{13}$ cm^3. This moderately high density is required to produce fluctuations in visible bremsstrahlung emission above the camera detection limit.

Throughout the time window in Fig. 2, the mode amplitude grows, which increases the coupling of the mode to the wall. The plasma rotation and TM mode frequency decrease due to the induced eddy currents that create magnetic fields that drag on the mode. The vertical lines in Fig. 2 are due to ELMs, which cause enhanced light emission as hot filaments are ejected into the scrapeoff layer (SOL) and interact with the outer wall.[2,15] The 4/2 harmonic is also visible in the spectrograms, and using a Fourier filtering technique, is imaged separately from the 2/1 structure as described below.

B. Temporal Fourier filtering of camera data

2D images of mode amplitude and phase are obtained by taking the Fourier transform of each pixel's time signal and retaining only the Fourier components in a narrow frequency range centered at the mode frequency.[14,16] This spectrally filtered image processing technique is a straightforward alternative to other techniques such as singular value decomposition.[17] Fourier filtering is applied during ELM-free discharges or between ELMs because the transient nature of ELMs produces a broad spectrum of Fourier components which corrupts the analysis of core MHD. Figures 3(a)–3(c) show the 2/1 normalized Fourier amplitude γ, phase ϕ, and mode structure (defined as $\gamma\sin\phi$) for filtered spectral power with frequency $f=2.0$ kHz and bandwidth of 78 Hz during a time window of 6.4 ms centered at $t=3450$ ms, as shown by the dashed vertical line in Fig. 2. The mode can be seen on both the low field side (right hand side of image) and the high field side of the magnetic axis, and the point of tangency between the camera line-of-sight and the magnetic axis is located near (x pixel, y pixel) $=(110,100)$. The amplitude image shows a null surface located near the island center at the $q=m/n=2$ surface located near $\rho=0.3$ on the low field side, and the phase image shows a π phase reversal at this same surface. These amplitude and phase features deviate from flux surfaces on the high field side due to line integration. The amplitude null surface and phase inversion are due to local pressure flattening near the center of the island, called the O point. For the standard case of the equilibrium pressure gradient directed toward the magnetic axis, this flattening inside the island creates a positive pressure perturbation outside the $q=2$ surface and a negative perturbation inside the $q=2$ surface. At the X point, the opposite occurs. Thus, at the exact center of an ideal island, the amplitude of the perturbation is zero and the phase reverses. The island-induced pressure perturbations cause changes to the bremsstrahlung emission mainly due to changes in the electron density because $\varepsilon_B\propto n_e^2Z_{\rm eff}/T_e^{1/2}$. The local emission perturbation due to rotating islands can be expressed as $\tilde{\varepsilon}_B\approx\zeta\cdot\nabla\varepsilon_B$, where ζ represents the field line radial displacement. Fourier filtering isolates the fluctuating

component of the emission and the processed signal is given by the line integrated perturbed bremsstrahlung emission $\delta\varepsilon_B = \int \tilde{\varepsilon}_B dl$.

Line integration complicates the measurement because all points along the viewing trajectory contribute to the signal. For pixels with a line of sight tangent to a high field side flux surface, each viewing ray passes through the high field side emission source once while passing through the low field side emission source twice (in front of and behind the ray's point of tangency). The contributions from these emission sources along the viewing ray can have opposite phases, resulting in a cancellation of the perturbation.

The spatial structure of the 4/2 harmonic shown in Figs. 3(d)–3(f) is obtained by Fourier filtering each pixel's time signal at the $n=2$ harmonic frequency $f=4.0$ kHz. These images are produced from the identical set of data as the 2/1 mode images. The 4/2 images demonstrate that the spectral filtering process can be used to identify separate spatial structures that simultaneously coexist in the plasma, provided that the frequencies associated with the structures do not overlap. The TM harmonic is a distortion of the 2/1 island due to nonlinear coupling in the island region. Measuring the harmonic distortions may be important for NTM control using a special class of external magnetic perturbations that couple to the stabilizing phase of the island evolution.[18,19] The harmonic spectral power is significantly lower compared with the power in the fundamental $n=1$ frequency, and thus the color scale for the harmonic amplitude images is reduced by a factor of 3 compared to the 2/1 images to maximize visibility. In Fig. 3(f), the $m=4$ structure is seen as the four positive and four negative emission perturbations as one follows a flux surface around a complete poloidal transit. These structures appear radially skewed due to the nonlinear distortion of the fundamental 2/1 island. In addition, filamentary structures caused by inter-ELM turbulence in the plasma edge are seen in D_α and CIII line emission outside of the $\rho=0.5$ contour; the actual radial location of these filaments is near $\rho=1.0$ and appears extended radially inward because the camera views the filaments wrapping around the edge of the plasma.

The evolution of the island structure seen three times during TM decay is shown in Figs. 4(c)–4(e). The data are mapped to the tangency points ($R_{\tan}$, $Z_{\tan}$) for each pixel, where R is the major radius and Z is the vertical coordinate with the midplane at $Z=0$. The structure immediately outside of the null point at the $q=2$ surface (here located at $\rho=0.4$) decreases in radial width as the island shrinks. Interestingly, the small island in Fig. 4(e) produces a large on-axis perturbation, but essentially no perturbation is observed outside the $q=2$ surface. This may be due to line integration or a flat emissivity profile and will be investigated in future research.

The structures rotate poloidally as the island rotates toroidally due to the helical structure of the island chain. The mode helicity follows the magnetic field helicity and is defined by B_T and I_p; ignoring any velocity of the mode relative to the $E_r=0$ plasma frame (where the plasma rotation makes the radial electric field zero), the poloidal direction of mode propagation depends on two factors: (1) the helicity and (2) the direction of toroidal plasma rotation ν_{rot}, assuming no

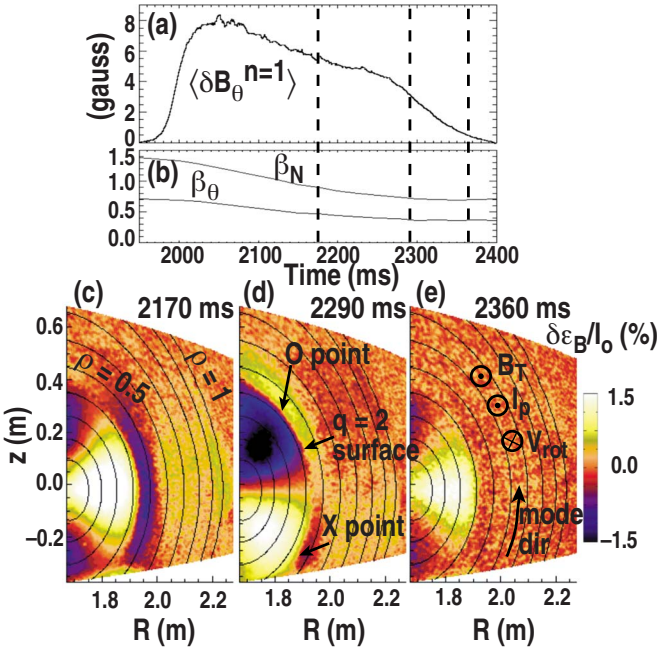

FIG. 4. (Color online) (a) The perturbed poloidal magnetic field due to a 2/1 island detected with a Mirnov coil for shot 131 364. (b) Normalized and poloidal beta decrease throughout mode evolution. [(c)–(e)] Images of $\gamma \sin(\phi)$ show the line-integrated perturbed bremsstrahlung emission $\delta\varepsilon_B$ normalized to the raw signal I_o near the magnetic axis. The times of the images correspond to the dashed lines in (a) and (b).

poloidal plasma rotation. Changing the direction of one or all three of the quantities B_T, I_p, and ν_{rot} will reverse the poloidal direction of mode propagation because either the helicity or the toroidal rotation direction will change. Reversing the direction of two of these quantities leaves the poloidal direction of the perturbation unchanged because either this will leave the helicity unchanged or will reverse both the helicity and toroidal rotation direction. Figure 4(e) shows the direction of these quantities along with the direction of poloidal mode propagation.

A midplane radial profile of the amplitude and phase of the Fourier filtered camera data is shown in Fig. 5. The amplitude profile has a local minimum located at the island center and the phase becomes inverted at this same location. This is expected because as the island rotates through the camera field of view, the perturbation caused by local pressure flattening at the O points is a minimum along the $q=2$ surface. Outside the island center, a peak in the perturbed amplitude is seen due to the finite island width.

C. Island width measurement

The island width w can be measured using ECE[20,21] if the plasma density is lower than the cutoff density, or inferred from Mirnov coils.[22] Here we use the camera to measure the island width w by measuring the distance d between the island center and the outer peak of the midplane amplitude profile. We then define the island width as $w \equiv 2d$ with the factor of 2 based on simple considerations of an island-induced pressure perturbation in a poloidal plane. The peak

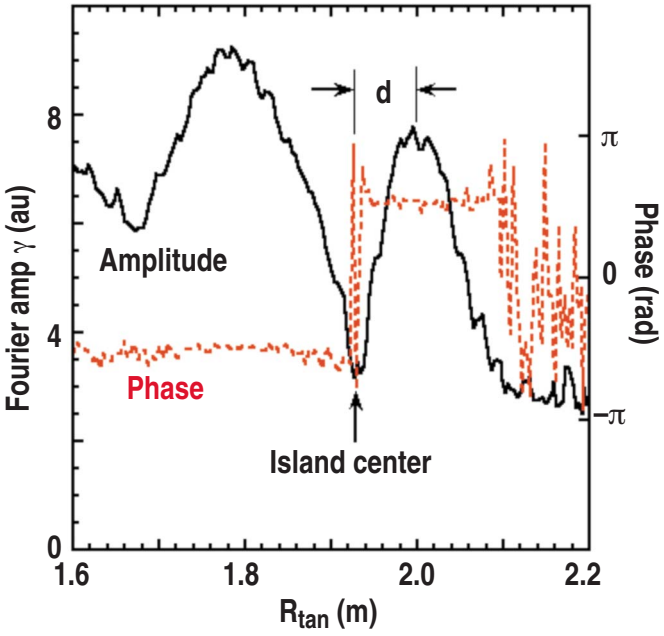

FIG. 5. (Color online) Midplane profile of the line-integrated amplitude γ and phase ϕ obtained by Fourier filtering at the mode frequency. At the island center, the fluctuation amplitude has a local minimum and the phase is inverted.

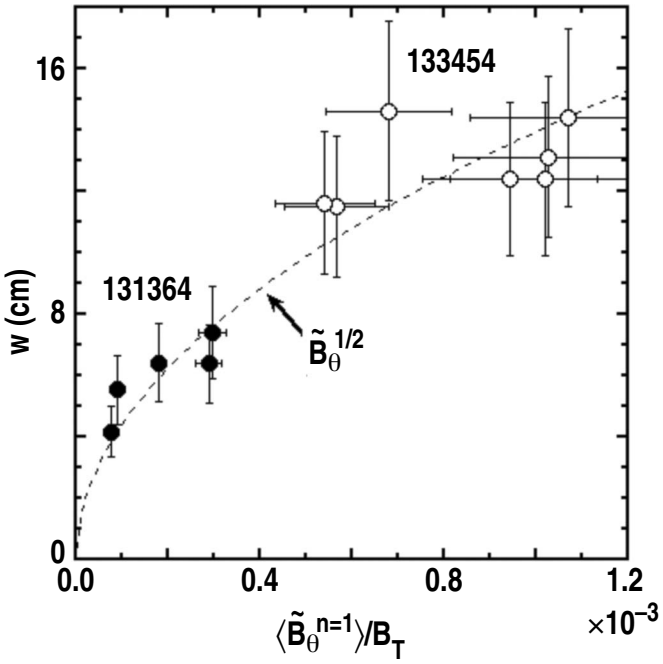

FIG. 6. Island widths w determined from camera measurements compared with the expected scaling from Ref. 22, shown as a dashed line.

on the inner side of the island center located at $R_{\tan}=1.78$ m in Fig. 5 is not used because the location of this inner peak is not well defined in all cases.

Figure 6 shows that the island width scaling determined from the camera data is in agreement with the predicted large aspect ratio cylindrical scaling for the perturbed poloidal magnetic field[22]

$$w \approx \left(\frac{8R_o b^{m+1} \langle \tilde{B}_\theta \rangle}{msB_T r_o^m} \right)^{1/2}, \quad (1)$$

where $\langle \tilde{B}_\theta \rangle$ is the amplitude of the m component of the fluctuating poloidal magnetic field measured at the vessel wall using a Mirnov magnetic probe located at minor radius b, and the magnetic shear is $s=r(dq/dr)/q^2$ (evaluated at the mode rational surface). The rational surface minor and major radii are defined as $r_o=(R_{\text{out}}-R_{\text{in}})/2$ and $R_o=(R_{\text{out}}+R_{\text{in}})/2$, respectively, where R_{in} and R_{out} are the minimum and maximum major radii of the rational surface, respectively. We assume that s, r_o, and R_o are constant for all the data points shown here. While the scaling agrees with the theoretical prediction, the factor of 2 used for the ratio w/d is ~50% too low compared to the expected width based on modeling and the measurements of the amplitude of the magnetic perturbation. This discrepancy may be due to the fact that Eq. (1) is strictly valid for a large aspect ratio cylindrical plasma and overestimates the width in a finite aspect ratio shaped plasma; in addition, there are significant uncertainties in the magnetic shear near the rational surface for this discharge. The discrepancy may also be a result of a shift in the apparent location of the outer peak to smaller major radii due to line integration.

Stabilization of NTMs has been demonstrated by replacing the missing bootstrap current using electron cyclotron current drive (ECCD) at the resonant surface.[23] Experiments in DIII-D show that the stabilization of the 2/1 NTM is very sensitive to the ECCD deposition location.[24] Maximum shrinkage of the island size occurred when co-ECCD was precisely aligned with the $q=2$ surface with the location of the rational surface determined from equilibrium reconstructions and fluctuations in the ECE at the island rotation frequency. In future devices with real-time output of fast camera data (the existing camera stores the data locally and is analyzed after each shot by downloading the data to a computer), fast imaging of island structure and location may provide a straightforward method of aiming ECCD in the island center without the need to rely on real-time equilibrium reconstruction.

D. Comparison to analytic model

The high spatial resolution and significant coverage of the plasma cross section allow detailed comparison to models. A simple analytic model of the local perturbed bremsstrahlung emission $\tilde{\varepsilon}_B$ is created by imposing a 2/1 island structure on the measured bremsstrahlung emission.[16] The emission profile is determined by inverting the axisymmetric signal measured with a calibrated radial array of 16 photodiodes that detect a narrow line-free region of the bremsstrahlung continuum spectrum at 5230 Å.[25] The island structure is given by the three-dimensional (3D) helical perturbed flux function[26] using the flux surface geometry from an equilibrium reconstruction. The model parameters for the perturbed poloidal flux are chosen to match the full island width

based on estimates from the amplitude of the perturbed poloidal magnetic field detected by an array of Mirnov probes.[22]

Inverting nonaxisymmetric camera data with finite signal to noise is nontrivial, resulting in amplification of noise and requiring assumptions about the underlying mode structure. Thus, a synthetic camera diagnostic has been developed[16] for forward modeling and is applied here to TMs. The synthetic camera simulates the line-integrating camera measurement along actual camera sightlines and simulates the finite exposure time of each frame, allowing direct comparison to the actual camera data.

Figure 7 shows the local perturbed bremsstrahlung emission $\tilde{\varepsilon}_B$ from the model and shows the fluctuation amplitude γ, phase ϕ, and mode structure $\gamma \sin(\phi)$ from the data and after applying the synthetic camera diagnostic to the model. A direct comparison between the true mode structure at a single poloidal plane and the camera-simulated, line-integrated calculation of the mode structure is shown in Figs. 7(a) and 7(d). The true mode structure appears more localized to a flux surface compared to the synthetic camera measurement, and the differences become more pronounced on the high field side. The actual camera view is limited to the outer portion of the midplane plasma cross section in the shot analyzed here; however, for the synthetic camera the simulated view is extended to include the high field side. The amplitude image shows similar features compared to the measurement with a full midplane cross section view, as shown in Fig. 3(a). Namely, there exist two regions on the high field side immediately above and below the midplane where the amplitude reduces to nearly zero. Line integration also causes the phase change on the high field side to appear less abrupt than the phase inversion at $q=2$ on the low field side. Comparing the mode structure $\gamma \sin(\phi)$ for both the model and the data shows an excellent agreement inside $\rho=0.6$; outside this radius a structure with opposite phase is seen in the data but not in the model. This motivated a comparison to a fully nonlinear simulation of island structure and evolution using NIMROD, which also failed to reproduce this outer structure. Our current hypothesis is that the structure outside $\rho=0.6$ is due to fluctuating line emission at the plasma edge resulting from island-induced surface deformation of the plasma edge.

E. Comparison to NIMROD modeling

The nonlinear, resistive, 3D code NIMROD[27] is used to simulate the nonlinear evolution of seed islands initialized with mode structure 2/1 at the $q=2$ surface. Discharge 131 364 is modeled using the equilibrium magnetic reconstruction and measured profiles of n_e, T_e, T_i, and f_{rot}. NIMROD solves extended MHD equations using a pseudospectral discretization in the toroidal direction, finite element discretization in the poloidal direction, and temporal advance with semi-implicit and implicit methods.

The $n=1-5$ magnetic and kinetic energies are shown in Fig. 8 and approach saturation after 7 ms. This time scale for island growth is approximately ten times faster than the growth time observed in the experiments (~50 ms) because

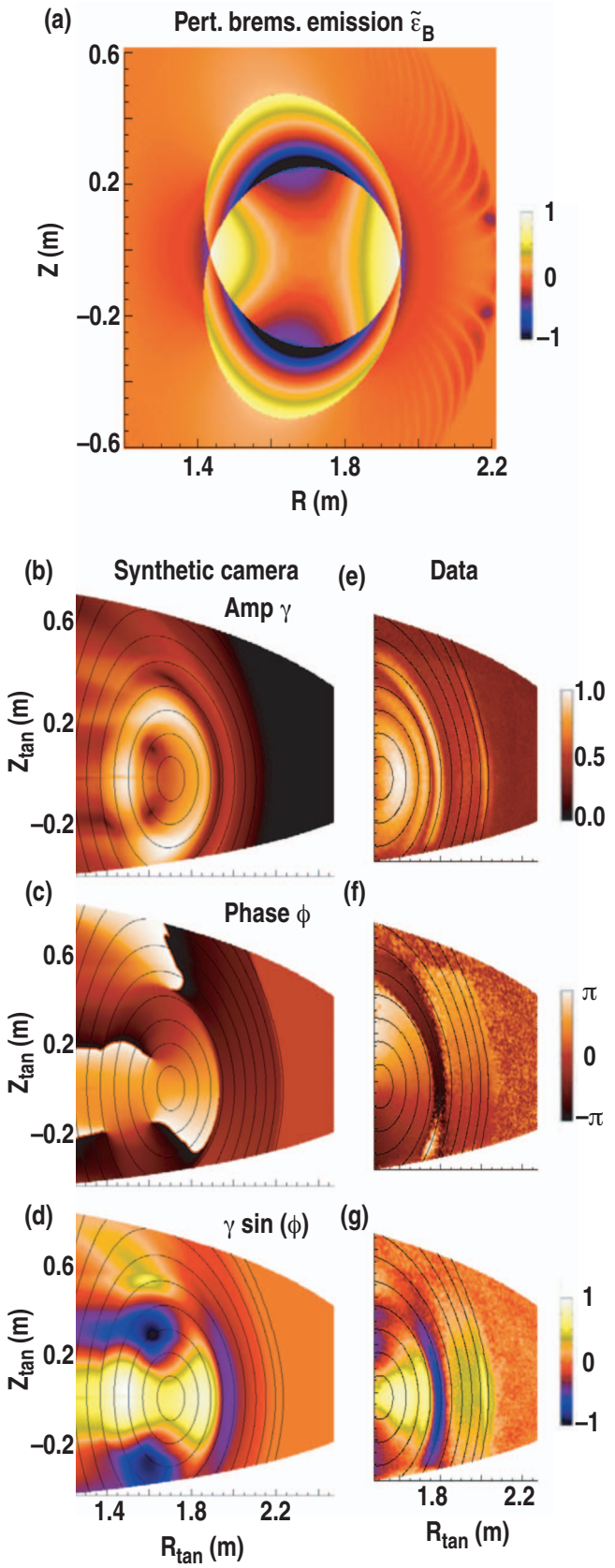

FIG. 7. (Color) (a) Model of island-induced perturbation of bremsstrahlung emission in a poloidal plane (no line integration). [(b)–(g)] Comparison of synthetic camera images to real camera data, where the synthetic camera images are obtained from the model shown in (a). The synthetic camera images [(b)–(d)] show a larger area than the experimental data [(e)–(g)].

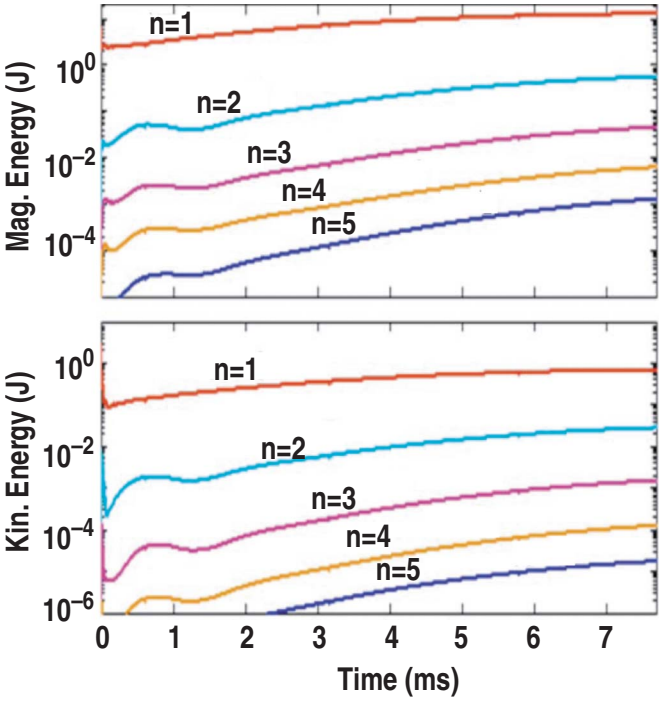

FIG. 8. (Color online) Magnetic and kinetic energy of toroidal mode numbers $n=1-5$ during the growth of the 2/1 seed island simulated using NIMROD.

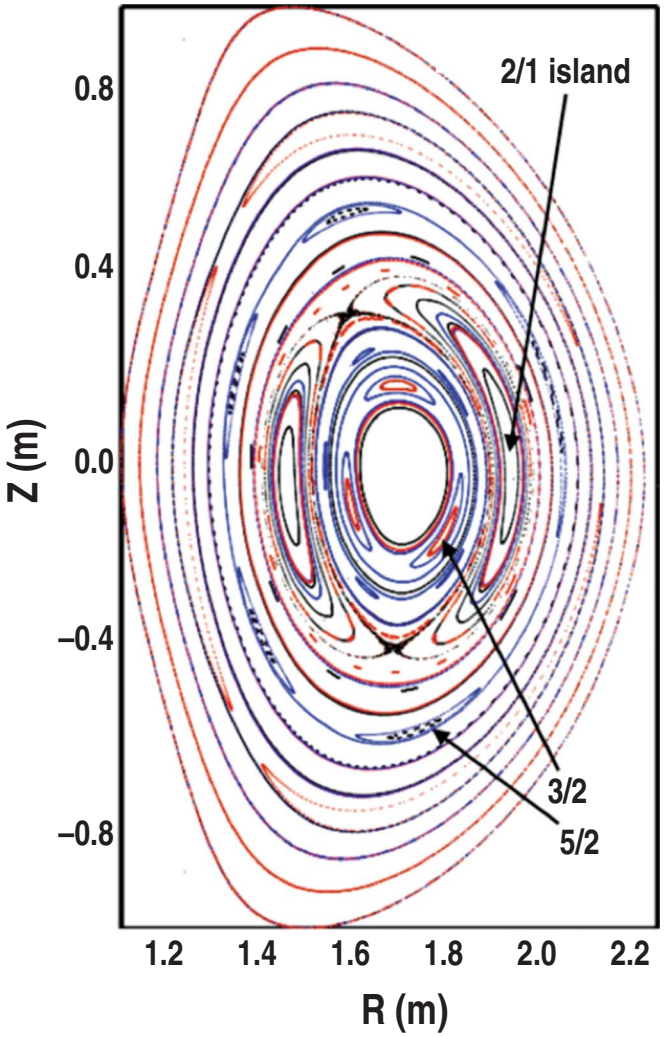

FIG. 9. (Color online) Poincare plot of magnetic field lines from the saturated state of the NIMROD simulation showing the dominant 2/1 island and other nonlinearly generated island structures.

the resistivity used in the simulation was approximately 100 times higher than that in the experiment. The only significant initially imposed perturbation in the simulation is the $n=1$ component. Harmonics are rapidly generated due to nonlinear evolution, and the magnitude of the $n=2$ magnetic energy is smaller than the $n=1$ energy by more than an order of magnitude. Figure 9 shows a Poincare plot of magnetic field lines at a given poloidal plane, where in addition to the dominant 2/1 island, 3/2, 5/3, and other nonlinearly generated island structures are visible.

The synthetic camera diagnostic is applied to the NIMROD simulation, and the results reproduce only the gross $m=2$ structure of the perturbed emission but miss the details seen in the camera image such as the structure with inverted phase outside the $q=2$ surface. The perturbed density $\tilde{n}_e$, temperature $\tilde{T}_e$, and bremsstrahlung emission $\tilde{\varepsilon}_B$ are line integrated along the synthetic camera sightlines that match the actual experiment. The perturbed emission is calculated as $\tilde{\varepsilon}_B=2n_eT_e^{-1/2}\tilde{n}_e-n_e^2T_e^{-3/2}\tilde{T}_e/2$ using equilibrium density n_e and temperature T_e. In the simulation, Z_{eff} is assumed to be constant with minor radius. Figure 10 shows that the 2D $\delta\varepsilon_B$ image closely follows the line integrated perturbed density and the 2D profile of the perturbed temperature is seen to resemble the experimental mode structure. A direct comparison of the NIMROD simulation to the camera data is seen in Figs. 10(c) and 10(d) and the agreement is rather poor. The lack of agreement between NIMROD modeling and the experiment may be due to an artificially large isotropic density diffusion of 10 m^2/s used in the simulation for numerical stability. This large density diffusion alters the density profile within the island by causing particles to fill in the island and prevents complete pressure flattening at the island O point, and thus washes out the island structure. Another possible cause of disagreement may be that the imposed 2/1 seed island starts the NIMROD simulation essentially in a nonlinear state, while the islands in the experiment evolve from a linearly unstable plasma. This difference between the simulated and experimental island evolutions may produce discrepancies in the final mode structures during the steady nonlinear state. In addition, the higher resistivity in the simulation could affect the saturated amplitude of the primary 2/1 island and the harmonics, which are important in determining the structure of the mode. The simulation also neglects two fluid and kinetic effects and fails to evolve the bootstrap current self-consistently.

IV. IMAGING THE SAWTOOTH INSTABILITY

In addition to TMs, detection of visible bremsstrahlung emission allows the study of sawtooth oscillations.[28] This transient instability with a 1/1 structure occurs when magnetic field lines break and reconnect due to peaked current at the plasma core. During the nonlinear phase of the instability known as the sawtooth crash, heat and particles are rapidly

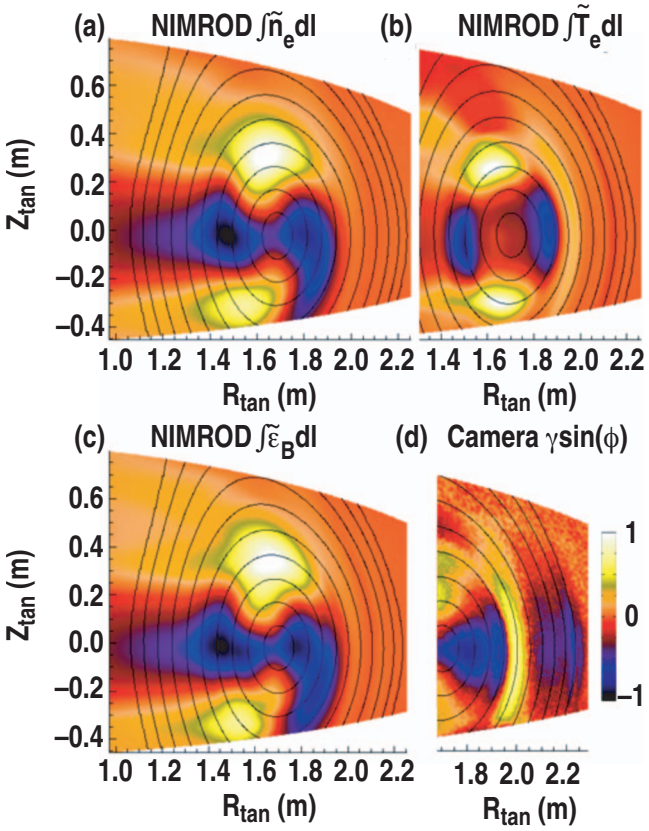

FIG. 10. (Color) Synthetic camera applied to NIMROD simulations showing line-integrated images of perturbations from (a) density, (b) electron temperature, and (c) perturbed bremsstrahlung emission. (d) Camera data of $\gamma \sin(\phi)$ which should be compared to image (c).

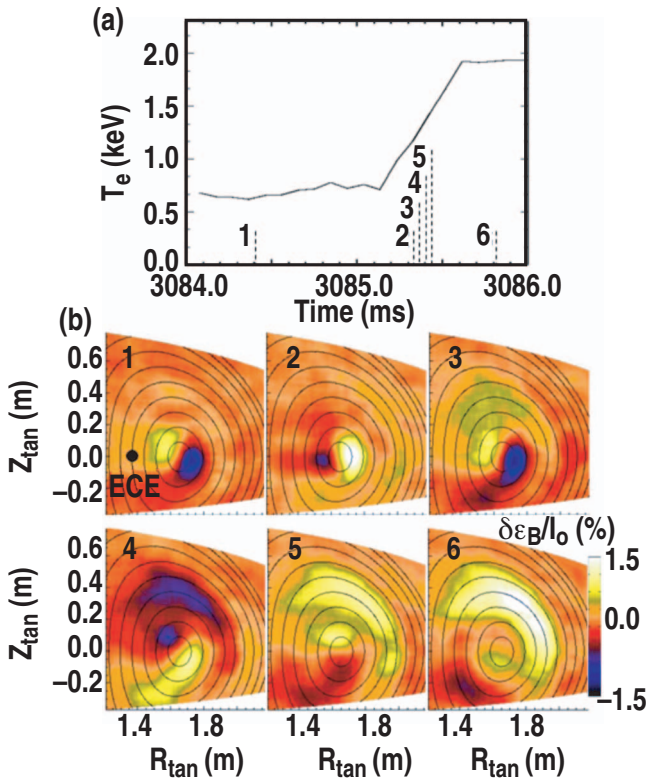

FIG. 11. (Color) (a) The electron temperature measured at a location near $\rho=0.4$ on the inboard midplane with the vertical lines marking the times of the images. (b) Snapshots of the 15 kHz component of the perturbed visible light during a sawtooth crash; all images have the same normalization, where I_o is the raw signal near the magnetic axis at the crash onset.

ejected from the core and mix with the surrounding plasma. The crash process occurs on a time scale of hundreds of microseconds, and after the crash the central temperature rises on a time scale of tens of milliseconds until the process repeats itself. During the crash, the core plasma can lose up to 15% of its stored energy.

Here we present the first visible light images of a sawtooth crash and point out the features that may be used to distinguish between various models. Multiple (~10) sawtooth oscillations are imaged in a *H*-mode bean-shaped plasma used to study stability limits,[29] and the camera images consistently show an $m=1$ precursor to the crash. The first two images of Fig. 11(b) show that the radial extent of this $m=1$ perturbation is localized near the center of the plasma where $\rho \leq 0.2$, presumably where $q<1$ (high density in this shot prevented accurate measurements of core current density). Following the crash, the radial extent of the perturbed emission is a significant fraction of the minor radius and consistently extends to $\rho>0.5$. We note that sawtooth crashes produce significant variation in the structure of the perturbed emission from one crash to the next. Since the camera views a finite toroidal region of the plasma, the measured emission would depend on the phase of the instability at the time of the crash. The $m=1$ precursor to the sawtooth crash was not observed previously in bean-shaped plasmas[29] possibly because the earlier plasmas were in a lower density regime and remained in *L*-mode. The data here were taken with $B_T=1.9$ T, reversed plasma current $I_p=1.5$ MA, NB heating of 2.7 MW, central electron temperature $T_e=2.5$ keV, and central density $n_e=7.5\times10^{13}$ cm^3.

Figure 11(a) shows a time sequence of T_e measured by the ECE diagnostic during one sawtooth crash. The vertical lines show the times of the images in Fig. 11(b). In the first image, the location of the T_e measurement is shown at $\rho=0.4$. The spatial structure of the line integrated perturbed emission is obtained by taking the fast Fourier transform (FFT) of every pixel's time series, retaining the frequency components at the $m=1$ mode frequency, and inverse Fourier transforming back to the time domain. The inverse transform is taken here because the spatial structure is not regular over the FFT time window of 2.5 ms, which spans the sawtooth crash, and thus interpreting the amplitude and phase images in the Fourier domain is not straightforward as in the case for rotating TMs. Here the frame rate is 26 kHz and the $m=1$ frequency is 15 kHz with a 1.5 kHz bandwidth used in the frequency filter. Despite the aliased measurement, Fourier filtering reveals clear structure throughout the sawtooth oscillation with $\delta\varepsilon_B/I_o$ in the range of $\pm1.5\%$, where I_o is the raw signal level at the magnetic axis.

The $m=1$ precursor oscillation remains localized inside the inversion radius for over 200 mode periods, where the inversion radius is inferred from the dynamics of the mode detected by the camera. The amplitude of the $m=1$ mode slowly grows during the precursor oscillations, and presumably when the perturbation grows large enough to cross the

$q=1$ surface the nonlinear crash phase is triggered. During the crash phase heat is quickly expelled from the core within a few hundred microseconds, and the temperature outside the $q=1$ surface rises by more than a factor of 2.5. The camera detects a rapid change in the structure of the perturbed emission. During and immediately after the crash the perturbed emission changes from a localized $m=1$ structure to a large $m=1$ crescent shape extending to over half the plasma minor radius. The crescent-shaped emission perturbation in the last two images of Fig. 11(b) is caused by transport of particles and heat from the core to the surrounding plasma. Determining whether the crescent shape is a hot structure or a cold island will require modeling to unfold the particle and heat contributions to the detected light signal.

Fast ECE imaging in TEXTOR shows cases where heat escapes from the core by puncturing the inversion radius at a poloidally localized hot spot.[30] The localized nature of the instability supports the idea of a pressure-driven ballooning mode, but the random poloidal location of the localized reconnection regions may indicate that secondary instabilities play a role in the crash process, since a pure ballooning type of mode would only be seen on the low field side. Fast imaging of visible emission, in combination with future modeling, could help investigate such phenomena in DIII-D and other tokamaks and may provide additional clues to the underlying mechanism of fast reconnection.

V. CONCLUDING REMARKS

Fast imaging of coherent and transient MHD activity in fusion plasmas is providing exciting insights into structure and dynamics. The detailed measurements of waves through direct visualization may allow the creation of more precise models to predict the behavior of future fusion reactors. Estimates of the signal levels in ITER predict that visible imaging will be an important diagnostic for core MHD activity,[16] as well as edge physics, and may be a powerful tool to steer ECCD for NTM control.

A synthetic camera, which simulates the actual camera view and finite exposure time of each frame, is used to compare the camera data to a simple analytic model of a 2/1 island structure, and good agreement is found inside the $q=2$ surface. Outside this surface, the camera data contain structure that is not seen in the model. This structure in the perturbed emission is most likely due to fluctuating line emission near the plasma edge caused by island-induced surface deformation of the plasma. Comparison of camera data to NIMROD modeling shows large discrepancies most likely due to the large density diffusion used in the code, which prevents complete pressure flattening through the island O point. The fast camera is used to measure the island width, and we find that the camera measurements agree with the predicted scaling of $w \propto \tilde{B}_{\theta}^{1/2}$.

The structure and dynamics of the perturbed emission during a sawtooth crash show that the $m=1$ precursor oscillation remains localized to minor radii inside the inversion radius for over 200 mode periods. During the nonlinear crash phase when the heat is expelled from the core, the perturbed emission extends to over half of the plasma minor radius. Plans for future work include detailed comparison of the detected emission with synthetic camera images of sawtooth models.

ACKNOWLEDGMENTS

This work was supported by the U.S. Department of Energy under Contract Nos. DE-FG02-07ER54917, DE-FC02-04ER54698, and DE-FG03-95ER54309.

The authors would like to thank N. H. Brooks, E. A. Lazarus, C. C. Petty, A. D. Turnbull, and E. J. Strait for useful discussions.

[1] A. Kirk, H. R. Wilson, G. F. Counsell, R. Akers, E. Arends, S. C. Cowley, J. Dowling, B. Lloyd, M. Price, and M. Walsh, Phys. Rev. Lett. **92**, 245002 (2004).
[2] J. H. Yu, J. A. Boedo, E. M. Hollmann, R. A. Moyer, D. L. Rudakov, and P. B. Snyder, Phys. Plasmas **15**, 032504 (2008).
[3] T. Eich, A. Herrmann, and J. Neuhauser, Phys. Rev. Lett. **91**, 195003 (2003).
[4] S. J. Zweben, R. J. Maqueda1, D. P. Stotler, A. Keesee, J. Boedo, C. E. Bush, S. M. Kaye, B. LeBlanc, J. L. Lowrance, V. J. Mastrocola, R. Maingi, N. Nishino, G. Renda, D. W. Swain, J. B. Wilgen, and NSTX Team, Nucl. Fusion **44**, 134 (2004).
[5] A. L. Roquemore, N. Nishino, C. H. Skinner, C. Bush, R. Kaita, R. Maqueda, W. Davis, A. Yu. Pigarov, and S. I. Krasheninnikov, J. Nucl. Mater. **363–365**, 222 (2007).
[6] J. H. Yu, D. L. Rudakov, A. Yu. Pigarov, R. D. Smirnov, N. H. Brooks, S. H. Muller, and W. P. West, J. Nucl. Mater. (in press).
[7] P. H. Rutherford, Phys. Fluids **16**, 1903 (1973).
[8] R. J. La Haye, Phys. Plasmas **13**, 055501 (2006).
[9] W. W. Heidbrink, E. D. Fredickson, T. K. Mau, C. C. Petty, R. I. Pinsker, M. Porkolab, and B. W. Rice, Nucl. Fusion **39**, 1369 (1999).
[10] D. Pacella, G. Pizzicaroli, M. Leigheb, R. Bellazzini, A. Brez, M. Finkenthal, D. Stutman, B. Blagojevic, R. Vero, R. Kaita, A. L. Roquemore, and D. Johnson, Rev. Sci. Instrum. **74**, 2148 (2003).
[11] S. Yamaguchi, H. Igami, H. Tanaka, and T. Maekawa, Phys. Rev. Lett. **93**, 045005 (2004).
[12] H. K. Park, N. C. Luhmann, A. J. Donné, I. G. Classen, C. W. Domier, E. Mazzucato, T. Munsat, M. J. van de Pol, Z. Xia, and TEXTOR Team, Phys. Rev. Lett. **96**, 195003 (2006).
[13] J. L. Luxon, Nucl. Fusion **42**, 614 (2002).
[14] J. H. Yu and M. A. Van Zeeland, Rev. Sci. Instrum. **79**, 10F516 (2008).
[15] D. L. Rudakov, J. A. Boedo, R. A. Moyer, P. C. Stangeby, J. G. Watkins, D. G. Whyte, L. Zeng, N. H. Brooks, R. P. Doerner, T. E. Evans, M. E. Fenstermacher, M. Groth, E. M. Hollmann, S. I. Krasheninnikov, C. J. Lasnier, A. W. Leonard, M. A. Mahdavi, G. R. McKee, A. G. McLean, A. Yu. Pigarov, W. R. Wampler, G. Wang, W. P. West, and C. P. C. Wong, Nucl. Fusion **45**, 1589 (2005).
[16] M. A. Van Zeeland, J. H. Yu, M. S. Chu, K. H. Burrell, R. J. La Haye, T. C. Luce, R. Nazikian, W. M. Solomon, and W. P. West, Nucl. Fusion **48**, 092002 (2008).
[17] C. E. Bush, B. C. Stratton, J. Robinson, L. E. Zakharov, E. D. Fredrickson, D. Stutman, and K. Tritz, Rev. Sci. Instrum. **79**, 10E928 (2008).
[18] R. Fitzpatrick and E. Rossi, Phys. Plasmas **8**, 2760 (2001).
[19] M. S. Chu, H. Ikezi, and T. H. Jensen, Phys. Fluids **27**, 472 (1984).
[20] Y. Nagayama, G. Taylor, E. D. Fredrickson, R. V. Budny, A. C. Janos, D. K. Mansfield, K. M. McGuire, and M. Yamada, Phys. Plasmas **3**, 2631 (1996).
[21] C. Ren, J. D. Callen, T. A. Gianakon, C. C. Hegna, Z. Chang, E. D. Fredrickson, K. M. McGuire, G. Taylor, and M. C. Zarnstorff, Phys. Plasmas **5**, 450 (1998).
[22] R. J. La Haye, R. J. Buttery, S. Guenter, G. T. A. Huysmans, M. Maraschek, and H. R. Wilson, Phys. Plasmas **7**, 3349 (2000).
[23] R. Prater, R. J. La Haye, J. Lohr, T. C. Luce, C. C. Petty, J. R. Ferron, D. A. Humphreys, E. J. Strait, F. W. Perkins, and R. W. Harvey, Nucl. Fusion **43**, 1128 (2003).

[24]C. C. Petty, R. J. La Haye, T. C. Luce, D. A. Humphreys, A. W. Hyatt, J. Lohr, R. Prater, E. J. Strait, and M. R. Wade, Nucl. Fusion **44**, 243 (2004).
[25]D. P. Schissel, R. E. Stockdale, H. St. John, and W. M. Tang, Phys. Fluids **31**, 3738 (1988).
[26]E. Strumberger, S. Gunter, E. Schwartz, and C. Tichmann, New J. Phys. **10**, 023017 (2008).
[27]C. R. Sovinec, A. H. Glasser, D. C. Barnes, T. A. Gianakon, R. A. Nebel, S. E. Kruger, D. D. Schnack, S. J. Plimpton, A. Tarditi, M. S. Chu, and NIMROD Team, J. Comput. Phys. **195**, 355 (2004).
[28]S. von Goeler, W. Stodiek, and N. Sauthoff, Phys. Rev. Lett. **33**, 1201 (1974).
[29]E. A. Lazarus, T. C. Luce, M. E. Austin, D. P. Brennan, K. H. Burrell, M. S. Chu, J. R. Ferron, A. W. Hyatt, R. J. Jayakumar, L. L. Lao, J. Lohr, M. A. Makowski, T. H. Osborne, C. C. Petty, P. A. Politzer, R. Prater, T. L. Rhodes, J. T. Scoville, W. M. Solomon, E. J. Strait, A. D. Turnbull, F. L. Waelbroeck, and C. Zhang, Phys. Plasmas **14**, 055701 (2007).
[30]T. Munsat, H. K. Park, I. G. J. Classen, C. W. Domier, A. J. H. Donne, N. C. Luhmann, Jr., E. Mazzucato, M. J. van de Pol, and TEXTOR Team, Nucl. Fusion **47**, L31 (2007).